Check for updates

Advanced Functional Materials

ADVANCED FUNCTIONAL MATERIALS
www.afm-journal.de

RESEARCH ARTICLE

Lanthanide-Doped Hybrid Metal Halide Glasses with Multidimensional Luminescence for X-Ray Imaging and Photonic Authentication

Shilin Jin[1] | Xiaoai Cao[1] | Luyao Wei[1] | Zhiqiong Wu[1] | Daqin Chen[1,2]

[1]College of Physics and Energy, Fujian Provincial Key Laboratory of Quantum Manipulation and New Energy Materials, Fujian Normal University, Fuzhou, Fujian, People's Republic of China | [2]Fujian Provincial Engineering Technology Research Center of Solar Energy Conversion and Energy Storage, Fuzhou, People's Republic of China

Correspondence: Daqin Chen (dqchen@fjnu.edu.cn)

Received: 24 August 2026 | **Revised:** 13 October 2026 | **Accepted:** 29 October 2026

Keywords: hybrid metal-halide glasses | lanthanide doping | multidimensional luminescence | photonic authentication | scintillators

ABSTRACT

Hybrid metal-halide glasses combine optical homogeneity and processability for scintillators, yet most reported systems rely on a single emissive center and conventional radiation-to-light conversion. Here, we report lanthanide (Ln)-doped BTP_2MnCl_4 (BTP^+ = Butyltriphenylphosphonium) hybrid glasses prepared by one-step melt-quenching, demonstrating expanded emission channels while preserving optical transparency and the amorphous state. Eu^{3+} is selected as a secondary emitter for its spectroscopic complementarity with Mn^{2+}. The glasses integrate broadband green Mn^{2+} emission with narrow red Eu^{3+} lines, whose relative contributions are regulated by Eu^{3+} content and excitation wavelength. Distinct thermal responses provide additional temperature modulation, while spectroscopic and time-resolved measurements support $Mn^{2+}\rightarrow Eu^{3+}$ energy transfer. As scintillators, the glasses achieve a light yield of 18 843 photons MeV^{-1}, a detection limit of 26.7 nGy_{air} s^{-1}, and an imaging resolution of 28.5 lp mm^{-1}, with stable radioluminescence under repeated and prolonged irradiation. Beyond conventional imaging, the composition-, excitation-, and temperature-dependent spectral responses enable photonic barcodes for sequential multilevel authentication. Furthermore, the successful preparation of Ln- and Sb-based glasses further demonstrates the generalizability of this glass-forming strategy. These results extend hybrid metal-halide glasses beyond conventional scintillation media toward spectrally addressable multifunctional materials, providing a route to integrate x-ray imaging with multidimensional optical information processing.

1 | Introduction

X-ray imaging relies on scintillators to convert high-energy ionizing radiation into detectable optical signals [1–4], with imaging quality determined by a balance among x-ray stopping power, luminescence efficiency, optical transparency, radiation stability, and processability. Conventional inorganic scintillators such as CsI:Tl, Gd_2O_2S:Tb, $Bi_4Ge_3O_{12}$, and $Lu_3Al_5O_{12}$:Ce (LuAG:Ce), offer strong radioluminescence and favorable optical properties but often require high-temperature crystal growth and complex processing [5], whereas organic scintillators are readily processable but suffer from limited x-ray attenuation because of their low effective atomic numbers [6, 7]. Recently, metal halide semiconductors, including perovskites and organic–inorganic hybrid systems [8–11], have provided an alternative platform owing to their high-Z constituents, tunable coordination environments, and excellent luminescent properties. However, many are obtained as microcrystals or powders that require incorporation into polymer matrices to form scintillation screens [12, 13]. Such composite screens typically require thicknesses of several

All rights reserved, including rights for text and data mining and training of artificial intelligence technologies or similar technologies.
© 2026 Wiley-VCH GmbH

hundred micrometers or even millimeters to ensure sufficient x-ray absorption and scintillation brightness. Unfortunately, thicker screens exacerbate light scattering and lateral photon spreading due to particle aggregation, refractive-index mismatch, and the abundance of crystal/polymer interfaces [14, 15]. This persistent trade-off between x-ray absorption and spatial resolution has therefore motivated the development of optically homogeneous scintillating media with reduced internal scattering.

In this context, organic–inorganic hybrid metal-halide (OIMH) glasses offer a distinct structural strategy by combining locally retained emissive units with a macroscopically homogeneous amorphous matrix [9, 16]. These local-order/long-range-disorder characteristics reduce grain boundaries and particle interfaces, and melt-quenching enables direct casting, molding, and large-area processing [15, 17], making them promising candidates for transparent scintillation screens. Importantly, the glass-forming ability and crystallization resistance are critical considerations for hybrid halide glass scintillators, as undesirable crystallization can introduce grain boundaries and refractive-index inhomogeneities, increasing optical scattering and lateral photon spreading and thereby compromising x-ray imaging resolution [14, 15, 17]. Previous organic side-chain engineering studies show that $(BUP)_2MnCl_4$ has a higher T_g/T_m ratio (0.76; T_m: melting temperatures; T_g: glass-transition temperatures) than $(BnO\text{-}MTP)_2MnCl_4$ (0.73) and $(ETP)_2MnCl_4$ (0.70), indicating favorable glass-forming characteristics despite its comparatively lower scintillation light yield [18]. These findings highlight the importance of balancing glass-forming ability and scintillation efficiency when selecting hybrid metal-halide hosts. Currently, OIMH glasses containing Mn^{2+}, Sb^{3+}, and Cu^{+} emissions have already demonstrated high-resolution x-ray imaging [14, 19, 20]. However, most reported systems rely on a single emissive center, which limits their spectral tunability. Lanthanide (Ln) ions offer a complementary route because their characteristic 4f–4f transitions yield multiple narrow emission lines at relatively fixed wavelengths and can open additional excitation and energy-transfer channels [21, 22]. Nevertheless, Ln-doped transition-metal hybrid glasses remain challenging, since differences in valence, coordination preference, and precursor chemistry may hinder homogeneous doping and glass formation while also introducing competing nonradiative pathways. To the best of our knowledge, Ln-doped transition-metal hybrid halide glasses have not yet been explored, presenting an opportunity to combine transparent scintillation imaging with richer, stimulus-dependent emission features.

Here, we develop Ln-doped BTP_2MnCl_4 (BTP^+ = Butyltriphenylphosphonium) hybrid glasses via a one-step melt-quenching approach to introduce additional emissive channels without sacrificing transparency and the amorphous state. Dy^{3+}-doped, Sm^{3+}-doped, and Eu^{3+}/Tb^{3+}-codoped BTP_2MnCl_4 glasses were successfully obtained, while the formation of related Dy^{3+}-, Sm^{3+}-, Eu^{3+}-, Tb^{3+}-, and Sb^{3+}-based glasses further demonstrates the generalizability of this glass-forming strategy. Among these systems, Eu^{3+} was selected as a representative secondary emitter for detailed investigation because of its marked spectroscopic complementarity with Mn^{2+}. Tetrahedrally coordinated Mn^{2+} provides broadband green emission that is sensitive to the local crystal field and lattice vibrations, whereas Eu^{3+} shows narrow red-emission channels with comparatively stable spectral positions. Importantly, the combination of crystal-field-sensitive Mn^{2+} $3d^5$ emission and characteristic Eu^{3+} 4f–4f transitions within a homogeneous amorphous matrix establishes spectrally complementary emission channels with distinct excitation and thermal responses. Photoluminescence excitation (PLE) spectra and time-resolved PL decay measurements support $Mn^{2+} \rightarrow Eu^{3+}$ energy transfer, while the relative contributions of the two emissive centers can be regulated through Eu^{3+} concentration, excitation wavelength, and temperature. This dual-center luminescence strategy thus enables multidimensional spectral modulation beyond that typically available in conventional single-emission-center (e.g., Mn^{2+}, Sb^{3+}, or Cu^{+}) OIMH glass scintillators. Meanwhile, the fabricated glasses retain efficient radioluminescence and high-resolution imaging, achieving a maximum light yield of 18 843 photons MeV^{-1}, an x-ray detection limit as low as 26.7 nGy_{air} s^{-1}, and an imaging resolution of 28.5 lp mm^{-1}. Furthermore, the composition-, excitation-, and temperature-dependent Mn^{2+}/Eu^{3+} spectral responses are converted into state-specific photonic barcodes for sequential multilevel authentication. Compared with previously reported OIMH glass scintillators that primarily rely on single-center emission and conventional x-ray-to-light conversion (Table S1), the present system combines competitive scintillation and imaging performance with dual-center multicolor emission, multidimensional spectral regulation, and photonic information encoding. These results extend the optical functionality of these OIMH glasses from scintillation imaging to multichannel information encoding.

2 | Results and Discussion

As illustrated in Figure 1a, BTPCl and $MnCl_2{\cdot}4H_2O$ were mixed at a molar ratio of 2:1 with varying amounts of $EuCl_3{\cdot}6H_2O$ and thoroughly ground to obtain a homogeneous precursor mixture. The mixture was then heated to produce a uniform transparent melt, cast into predesigned silicone molds, and rapidly cooled to room temperature. This process enables direct shaping of the glasses into macroscopic digits and letters with controlled dimensions. Under 365 nm ultraviolet (UV) irradiation, the "2026 AFM" glass samples exhibit continuously tunable emission colors from green to red, demonstrating effective modulation of the luminescence through Eu^{3+} incorporation.

To gain clearer insight into the local coordination structure in the glasses, BTPCl and BTP_2MnCl_4 single crystals were prepared by a solvothermal crystallization method, as described in the Supporting Information. Single-crystal x-ray diffraction (SCXRD) analysis reveals that BTPCl crystallizes in the monoclinic $P2_1/c$ space group, with unit-cell parameters of a = 11.2028(4) Å, b = 10.0307(1) Å, c = 17.3353(3) Å, V = 1893.04(6) $Å^3$, and Z = 4. By contrast, BTP_2MnCl_4 crystallizes in the orthorhombic *Pbcn* space group, with unit-cell parameters of a = 33.4420(7) Å, b = 16.4704(3) Å, c = 16.0265(2) Å, V = 8827.4(3) $Å^3$, and Z = 8. The corresponding crystallographic parameters are summarized in Table S2. As shown in Figure 1b, BTP_2MnCl_4 adopts a typical zero-dimensional organic–inorganic hybrid structure in which isolated $[MnCl_4]^{2-}$ tetrahedral units are effectively separated by bulky BTP^+ organic cations and arranged periodically within the lattice. The enlarged view in Figure 1b further displays the molecular configuration of the BTP^+ cation and the

16163028, 0, Downloaded from https://advanced.onlinelibrary.wiley.com/doi/10.1002/adfm.79493 by Daqin Chen - Zhongshan University , Wiley Online Library on [05/11/2026]. See the Terms and Conditions (https://onlinelibrary.wiley.com/terms-and-conditions) on Wiley Online Library for rules of use; OA articles are governed by the applicable Creative Commons License

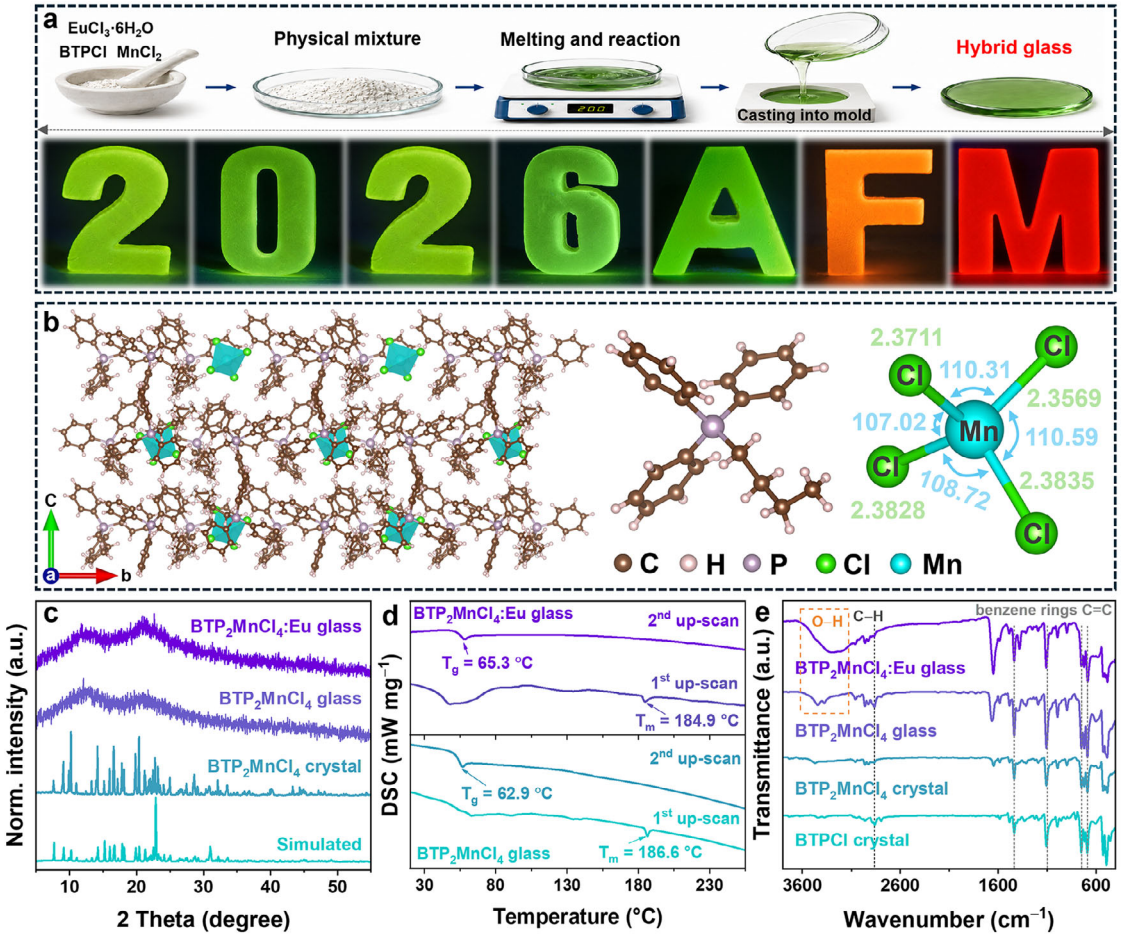


FIGURE 1 | Preparation and structural characterization of BTP_2MnCl_4:Eu hybrid glasses. (a) Schematic illustration of the one-step melt-quenching process and photographs of BTP_2MnCl_4:Eu glasses shaped into numbers and letters under 365 nm irradiation. (b) Crystal structure of BTP_2MnCl_4, molecular structure of the BTP^+ cation, and coordination geometry of the $[MnCl_4]^{2-}$ tetrahedron with selected Mn–Cl bond lengths and Cl–Mn–Cl bond angles. Units are Å and degrees. Color code: C, brown; H, pink; P, grayish purple; Cl, green; Mn, cyan. (c) Simulated XRD pattern of BTP_2MnCl_4 derived from SCXRD data and experimental PXRD patterns of BTP_2MnCl_4 crystal, BTP_2MnCl_4 glass, and BTP_2MnCl_4:Eu glass. (d) First up-scan and second up-scan DSC curves of BTP_2MnCl_4 and BTP_2MnCl_4:Eu glasses. (e) ATR-FTIR spectra of BTPCl crystal, BTP_2MnCl_4 crystal, BTP_2MnCl_4 glass, and BTP_2MnCl_4:Eu glass.

coordination geometry of the $[MnCl_4]^{2-}$ unit. In this motif, each Mn^{2+} center is coordinated by four Cl^- ions. The unequal Mn–Cl bond lengths and the deviation of the Cl–Mn–Cl angles from ideal tetrahedral values indicate slight distortion of the coordination geometry (Table S3). Notably, the shortest Mn^{2+}–Mn^{2+} separation in BTP_2MnCl_4 exceeds 10.2 Å (Figure S1), which is much larger than the Mn–Cl bond lengths, suggesting weak electronic coupling and negligible spin-exchange interactions between adjacent inorganic units [23, 24]. This spatial isolation limits excitation-energy migration among Mn^{2+} centers [9, 25], thereby reducing the probability of concentration-quenching and associated nonradiative losses.

The experimental powder XRD (PXRD) patterns of the BTPCl and BTP_2MnCl_4 crystals exhibit characteristic diffraction reflections at positions generally consistent with those simulated from their corresponding single-crystal structures (Figure 1c and Figure S2), supporting the formation of the expected crystalline phases. The observed differences in relative peak intensities may arise from preferred orientation effects associated with crystallite morphology and sample preparation. In contrast, the melt-quenched BTP_2MnCl_4 and BTP_2MnCl_4:Eu glasses display only broad diffuse scattering features. No crystalline diffraction peaks are detected across the series with different Eu^{3+} contents (Figure S3), indicating that Eu^{3+} incorporation does not induce detectable crystallization and that the amorphous state is retained throughout the investigated composition range. Differential scanning calorimetry (DSC) measurements were further conducted to evaluate the thermal behavior and crystallization resistance of the glasses. Neither the pristine nor the Eu^{3+}-doped BTP_2MnCl_4 glasses exhibit a distinct crystallization exotherm during heating (Figure 1d). Their T_m values are 186.6°C and 184.9°C, respectively, while the corresponding T_g values are 62.9°C and 65.3°C, giving T_g/T_m values of 0.73 and 0.74. Both ratios exceed the empirical threshold of 2/3 [16, 17, 26], indicating favorable glass-forming ability and strong resistance to crystallization. Consistently, in situ temperature-dependent PXRD measurements reveal no detectable crystalline phase over the examined temperature range (Figure S4), further supporting the thermal stability of the amorphous structures.

16163028, 0, Downloaded from https://advanced.onlinelibrary.wiley.com/doi/10.1002/adfm.79493 by Daqin Chen - Zhongshan University , Wiley Online Library on [05/11/2026]. See the Terms and Conditions (https://onlinelibrary.wiley.com/terms-and-conditions) on Wiley Online Library for rules of use; OA articles are governed by the applicable Creative Commons License

The attenuated total reflectance Fourier-transform infrared (ATR-FTIR) spectra of BTPCl crystal, BTP_2MnCl_4 crystal, and the corresponding glasses retain the characteristic vibrations of the BTP^+ cation [22, 27], including the C–H stretching modes near 3000 cm^{-1} and the aromatic C═C stretching modes around 1600 cm^{-1} (Figure 1e). The preservation of these vibrational signatures indicates that the basic molecular structure of the organic cation remains intact during melt quenching. A broader O–H stretching band emerges in the Eu^{3+}-doped glass over the 3200–3600 cm^{-1} region [28, 29], consistent with water introduced by the hydrated $EuCl_3{\cdot}6H_2O$ precursor. These high-frequency O–H vibrations may also facilitate multi-phonon relaxation of the Eu^{3+} $^5D_0$ excited state, introducing an additional nonradiative quenching pathway. To further investigate the structural influence of Eu^{3+} doping, Raman spectroscopy was performed on pristine and Eu^{3+}-doped BTP_2MnCl_4 glasses (Figure S5). The Raman spectra exhibit highly similar vibrational features, with the characteristic vibrations of the BTP^+ organic cations well preserved after Eu^{3+} incorporation. Meanwhile, no additional Raman bands attributable to a separate $EuCl_3{\cdot}6H_2O$ phase are observed. This spectral similarity indicates that Eu^{3+} doping does not substantially change the dominant vibrational characteristics of the hybrid glass. Considering the zero-dimensional structure of BTP_2MnCl_4, in which isolated $[MnCl_4]^{2-}$ tetrahedra are spatially separated by bulky organic cations, local accommodation of Eu-containing species can occur without significantly perturbing the overall structural characteristics of the glass. Energy-dispersive x-ray spectroscopy (EDX) and elemental mapping reveal uniform distributions of P, Mn, Cl, and Eu in the glass (Figures S6 and S7). The measured P:Mn:Cl:Eu molar ratio of 24.59:13.92:60.43:1.06 is broadly consistent with the expected composition. X-ray photoelectron spectroscopy (XPS) further confirms the incorporation of Eu^{3+} ions into the BTP_2MnCl_4 glass, as evidenced by the characteristic P 2p, Mn 2p, Cl 2p, and Eu 3d/4d signals (Figure S8). With increasing Eu^{3+} content, the relative intensity of the Mn 2p signals gradually decreases, whereas the characteristic Eu 3d/4d signals become progressively stronger. Meanwhile, the Mn 2p binding energies remain essentially unchanged, indicating that the predominant chemical state of Mn is preserved after Eu^{3+} doping. Together with the homogeneous elemental distribution, preserved Raman and ATR-FTIR vibrational features, and absence of detectable crystalline impurity phases, these results support the successful incorporation of Eu^{3+} into the amorphous hybrid glass without substantial disruption of its original structural characteristics.

Pristine BTP_2MnCl_4 glass exhibits a broadband green emission centered at 530 nm with a full width at half-maximum (FWHM) of 73 nm and a decay lifetime of 1.65 ms (Figure S9a,b). These characteristics are consistent with the $^4T_1(G)\rightarrow{}^6A_1$ transition of tetrahedrally coordinated Mn^{2+} [16, 24]. The time-resolved emission spectra acquired within time windows from 0.2 to 9.9 ms retain an essentially unchanged peak position and spectral profile (Figure S9c), while the excitation-emission map converges on the same emission band under different excitation regions (Figure S9d), indicating that the green luminescence predominantly originates from a common Mn^{2+} emissive state.

Under 360 nm excitation, the incorporation of Eu^{3+} progressively modifies the emission composition of the glass (Figure 2a). As the nominal $EuCl_3{\cdot}6H_2O$ doping concentration increases, the broadband emission of Mn^{2+} is gradually suppressed, accompanied by the emergence of sharp Eu^{3+} emission lines at ~593, 612/619, 653, and 702 nm. These bands are assigned to the $^5D_0\rightarrow{}^7F_1$, $^5D_0\rightarrow{}^7F_2$, $^5D_0\rightarrow{}^7F_3$, and $^5D_0\rightarrow{}^7F_4$ transitions, respectively [27, 30]. Both time-resolved emission spectra and PL decay curves provide evidence for the coexistence of two emitting centers (Figure S10). The Eu^{3+} emission reaches a maximum at a nominal addition of 0.3 mmol and decreases under further Eu^{3+} incorporation, consistent with the onset of concentration quenching (Figure S11). The actual Eu^{3+} concentrations were determined by inductively coupled plasma-mass spectrometry (ICP-MS), with the Eu molar percentage defined relative to the total Mn and Eu metal contents. The samples prepared with nominal $EuCl_3{\cdot}6H_2O$ additions of 0.1, 0.3, and 0.5 mmol exhibit actual Eu^{3+} concentrations of 1.50, 3.97, and 7.37 mol%, respectively (Table S4). The integrated PL intensities of the BTP_2MnCl_4 and BTP_2MnCl_4:Eu glasses show a linear dependence on excitation power (Figure 2b and Figure S12), accompanied by invariant spectral profiles. This behavior unequivocally rules out emission from defect or trap states and corroborates an intrinsic radiative recombination process. The PL quantum yield (PLQY) values of the pristine BTP_2MnCl_4 glass and the BTP_2MnCl_4:Eu glass containing 7.37 mol% Eu were determined to be 41.5% and 20.9%, respectively (Figure 2c).

The International Commission on Illumination (CIE) chromaticity coordinates further demonstrate that, with increasing Eu^{3+} doping content, the luminescence color systematically shifts from the Mn^{2+}-dominated green region to the Eu^{3+}-dominated orange-red and red region (Figure 2d). Beyond compositional control, both the 0.3 and 1.0 mmol Eu^{3+}-doped glasses exhibit marked excitation-wavelength-dependent luminescence (Figure 2e,f). The two-dimensional excitation-emission maps (Figure S13) confirm that while Mn^{2+} broadband and Eu^{3+} narrow-band emissions in the 0.3 mmol sample, the Eu^{3+} channel overwhelmingly outcompetes Mn^{2+} at 1.0 mmol. This excitation-tunable population balance between the two emitters thus allows continuous color modulation. The PL excitation (PLE) spectra monitored at different emission wavelengths further reveal the excitation pathways of Mn^{2+} and Eu^{3+} centers (Figure 2g,h). The pristine BTP_2MnCl_4 glass exhibits broad Mn^{2+} d–d excitation bands, which are assigned to transitions from the $^6A_1$ ground state to the $^4E(D)$, $^4T_2(D)$, $^4E/^4A_1(G)$, $^4T_2(G)$, and $^4T_1(G)$ excited states [16, 24]. After Eu^{3+} doping, the PLE spectra monitored at the Eu^{3+} characteristic emissions contain sharp 4f–4f excitation peaks together with broad responses corresponding to the Mn^{2+} excitation bands. This spectral correlation indicates that Eu^{3+} emission can be populated either through direct excitation of its own intrinsic levels or indirectly through Mn^{2+}-related excited states, providing spectroscopic evidence for Mn^{2+}-to-Eu^{3+} energy transfer. The PL decay dynamics further support this process. As the nominal $EuCl_3{\cdot}6H_2O$ addition increases from 0 to 1.0 mmol, the Mn^{2+} lifetime monitored at 530 nm progressively shortens from 1.65 to 1.29, 1.11, 0.68, and 0.58 ms (Figure 2i), yielding energy-transfer efficiencies of 21.8%, 32.7%, 58.8%, and 64.9%, respectively (Figure S14). Collectively, these results demonstrate that Eu^{3+} incorporation introduces characteristic narrowband 4f–4f emission channels and additional excitation pathways into the Mn^{2+}-based hybrid glass. Combined with $Mn^{2+}\rightarrow Eu^{3+}$ energy transfer, the complementary broadband green Mn^{2+}

16163028, 0, Downloaded from https://advanced.onlinelibrary.wiley.com/doi/10.1002/adfm.79493 by Daqin Chen - Zhongshan University , Wiley Online Library on [05/11/2026]. See the Terms and Conditions (https://onlinelibrary.wiley.com/terms-and-conditions) on Wiley Online Library for rules of use; OA articles are governed by the applicable Creative Commons License

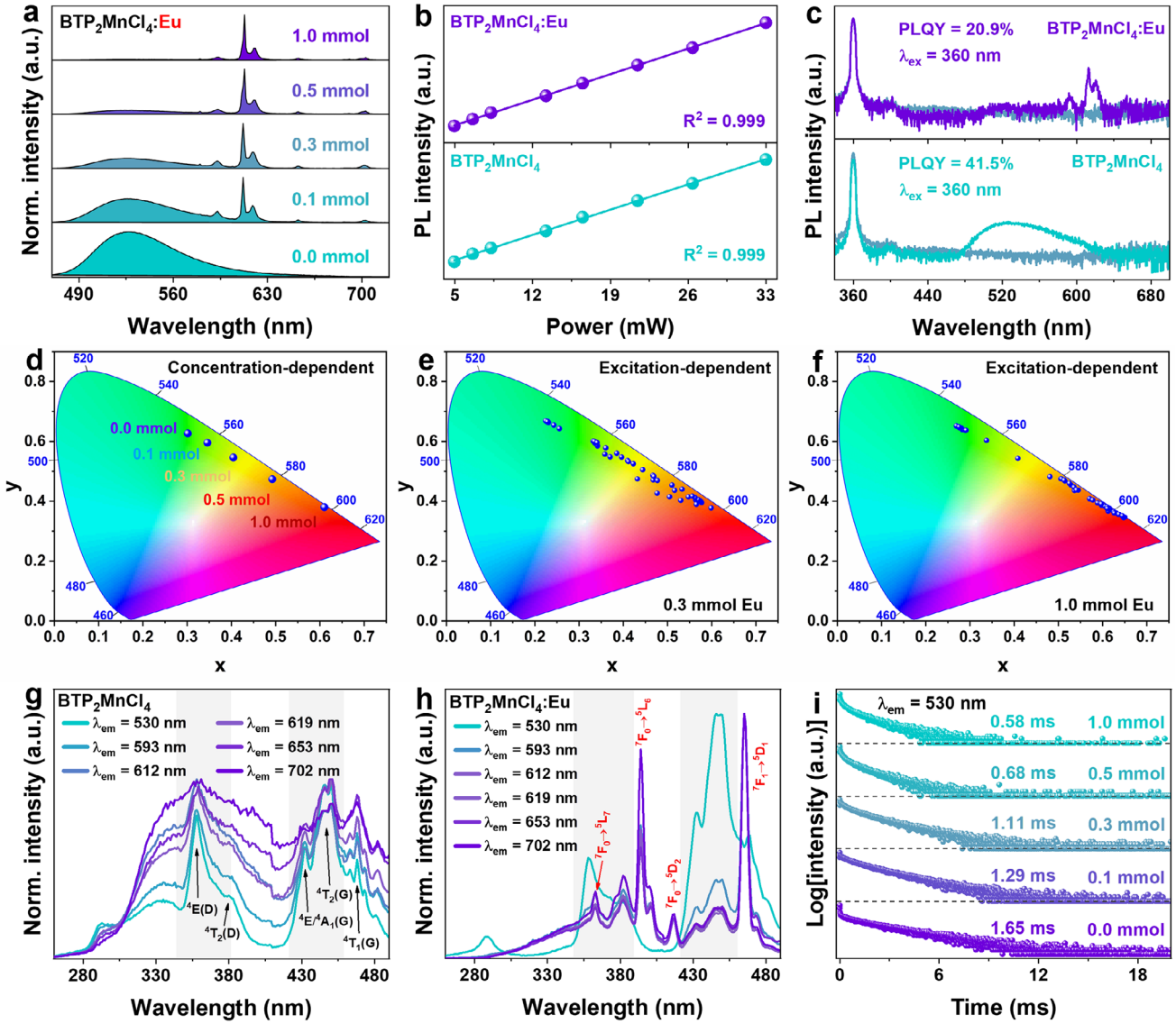


FIGURE 2 | Composition- and excitation-dependent photoluminescence of BTP_2MnCl_4:Eu glasses. (a) Normalized PL spectra of BTP_2MnCl_4:Eu glasses with nominal $EuCl_3{\cdot}6H_2O$ additions of 0–1.0 mmol under 360 nm excitation. (b) Integrated PL intensities of BTP_2MnCl_4 and BTP_2MnCl_4:Eu glasses as a function of excitation power. (c) PL spectra and corresponding PLQY values of BTP_2MnCl_4 and BTP_2MnCl_4:Eu glasses under 360 nm excitation. (d) CIE chromaticity coordinates of BTP_2MnCl_4:Eu glasses with different Eu^{3+} contents. (e,f) Excitation-wavelength-dependent CIE chromaticity coordinates of BTP_2MnCl_4:Eu glasses with nominal $EuCl_3{\cdot}6H_2O$ additions of 0.3 mmol (e) and 1.0 mmol (f). (g,h) Normalized PLE spectra of BTP_2MnCl_4 (g) and BTP_2MnCl_4:Eu (h) glasses monitored at 525, 593, 612, 619, 653, and 702 nm. (i) PL decay curves by monitoring Mn^{2+} emission at 530 nm for BTP_2MnCl_4:Eu glasses with nominal $EuCl_3{\cdot}6H_2O$ additions of 0–1.0 mmol.

and sharp red Eu^{3+} emissions enable composition- and excitation-wavelength-dependent spectral regulation, providing the foundation for subsequent multidimensional luminescence modulation.

To elucidate the thermal responses of the two emissive centers in BTP_2MnCl_4:Eu glass and their influence on the luminescence color, temperature-dependent PL spectra were investigated across 80–290 K. Under 360 nm excitation, the Mn^{2+} emission of pristine BTP_2MnCl_4 progressively decreases with increasing temperature (Figure 3a). Upon incorporation of 3.97 mol% Eu, the Mn^{2+} broad-band and Eu^{3+} sharp-line emissions coexist but exhibit distinct thermal decay behaviors (Figure 3b). The activation energies extracted from the temperature-dependent Mn^{2+} emission of the undoped glass are 72.3 meV, while the corresponding values for the Mn^{2+} and Eu^{3+} emissions of the 3.97 mol% Eu-doped glass increase to 98.1 and 98.4 meV, respectively (Figure 3c,d), indicating a higher barrier against thermal quenching at the intermediate Eu^{3+} content. With a further increase in Eu content to 7.37 mol%, the activation energies of the Mn^{2+} and Eu^{3+} emissions decrease to 69.5 and 60.4 meV, respectively (Figure S15), which is consistent with the concentration-quenching behavior observed at higher Eu^{3+} concentrations and suggesting enhanced nonradiative energy loss under excessive doping.

The pronounced temperature sensitivity of Mn^{2+} luminescence is closely associated with the local structural disorder induced by vitrification. Upon transition from the crystalline to the glassy

16163028, 0, Downloaded from https://advanced.onlinelibrary.wiley.com/doi/10.1002/adfm.79493 by Daqin Chen - Zhongshan University , Wiley Online Library on [05/11/2026]. See the Terms and Conditions (https://onlinelibrary.wiley.com/terms-and-conditions) on Wiley Online Library for rules of use; OA articles are governed by the applicable Creative Commons License

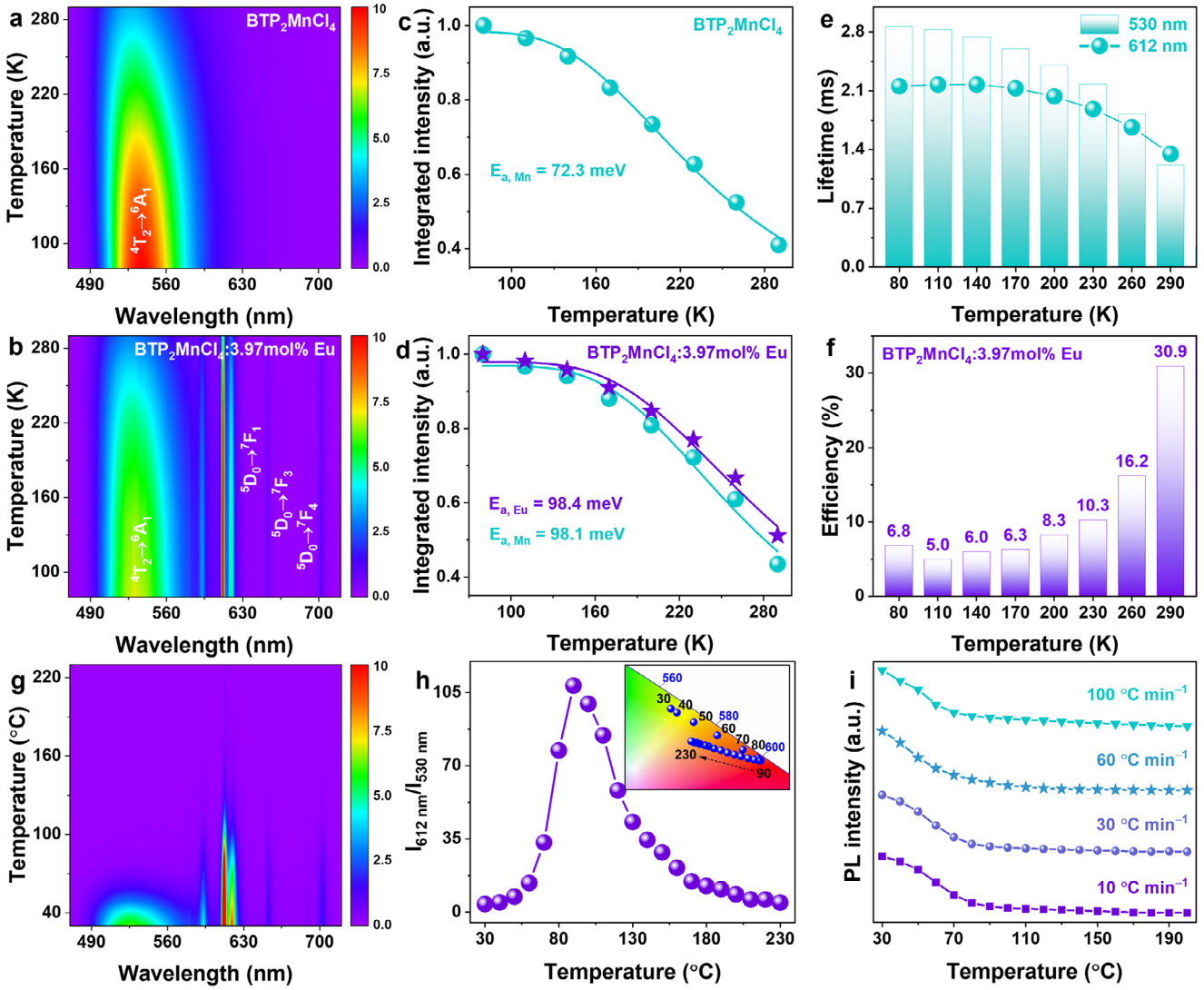


FIGURE 3 | Thermal regulation of Mn^{2+}/Eu^{3+} dual emission in BTP_2MnCl_4:Eu glasses. (a,b) Temperature-dependent PL contour maps of BTP_2MnCl_4 glass (a) and BTP_2MnCl_4:Eu glass containing 3.97 mol% Eu (b) under 360 nm excitation. (c,d) Temperature-dependent integrated PL intensities and corresponding Arrhenius fits of BTP_2MnCl_4 glass (c) and BTP_2MnCl_4:Eu glass containing 3.97 mol% Eu (d). (e) Temperature-dependent PL lifetimes of BTP_2MnCl_4:Eu glass containing 3.97 mol% Eu monitored at 530 and 612 nm. (f) Temperature-dependent transfer efficiency from Mn^{2+} to Eu^{3+} for BTP_2MnCl_4:Eu glass with 3.97 mol% Eu. (g) Temperature-dependent PL contour map of BTP_2MnCl_4:Eu glass containing 3.97 mol% Eu from 30°C to 230°C under 360 nm excitation. (h) Temperature-dependent $I_{612\,nm}/I_{530\,nm}$ intensity ratio and corresponding CIE chromaticity coordinates. (i) Temperature-dependent PL intensities recorded under 360 nm excitation at different heating rates of 10, 30, 60, and 100°C min^{-1}.

state, the Mn^{2+} emission in BTP_2MnCl_4 shifts to lower energy and becomes substantially broader (Figure S16). The Huang-Rhys factors increase from 3.6 for the crystal to 7.3 for the glass, with corresponding phonon energies of 51.2 and 42.3 meV, respectively (Figures S17 and S18), revealing markedly enhanced electron-phonon coupling in the amorphous state [14, 31]. With increasing temperature, the Mn^{2+} emission gradually blueshifts, whereas the characteristic Eu^{3+} lines remain essentially unchanged in position (Figure S19a,b). This disparity reflects the different sensitivities of the two electronic configurations to their local environments: the $^4T_1(G)$ excited state of Mn^{2+} is directly modulated by the crystal field, while the 4f electrons of Eu^{3+} are effectively shielded by the outer 5s and 5p orbitals [9, 17, 22, 32]. Furthermore, the Eu^{3+} emission in BTP_2MnCl_4:Eu glass also remains stable at peak positions under 393 nm excitation (Figure S19c), further corroborating the intrinsic spectral robustness of its 4f–4f transitions. To further quantify the distinct thermal responses of the two emission bands, we measured temperature-dependent PL decay curves (Tables S5 and S6). The lifetimes monitored at 530 nm (Mn^{2+}) and 612 nm (Eu^{3+}) progressively shorten as the temperature increases from 80 to 290 K (Figure 3e and Figure S20), indicating increasingly active thermally assisted nonradiative decay. Remarkably, the $Mn^{2+}\rightarrow Eu^{3+}$ energy transfer efficiency remains ~5%–7% between 80 and 170 K but increases markedly at higher temperatures, reaching 30.9% at 290 K (Figure 3f). This evolution indicates strengthened energetic coupling between Mn^{2+} and Eu^{3+} toward room temperature, which contributes to the redistribution of excitation energy between the two emission channels. Consistently, the intensity ratio of $I_{612\,nm}/I_{530\,nm}$ increases from ~2.0 to 2.6 in the 80–290 K range (Figure S21), reflecting the increasing relative contribution of Eu^{3+} emission under heating.

16163028, 0, Downloaded from https://advanced.onlinelibrary.wiley.com/doi/10.1002/adfm.79493 by Daqin Chen - Zhongshan University , Wiley Online Library on [05/11/2026]. See the Terms and Conditions (https://onlinelibrary.wiley.com/terms-and-conditions) on Wiley Online Library for rules of use; OA articles are governed by the applicable Creative Commons License

To examine the dual-emission response over a wider temperature range, we extended the measurements from 30°C to 230°C. As shown in Figure 3g, the Mn^{2+} broadband emission rapidly decays during the initial stage of heating, whereas the Eu^{3+} emission persists to higher temperatures. Their different quenching rates lead to a pronounced evolution of the emission color. Below 100°C, the intensity ratio of $I_{612\,nm}/I_{530\,nm}$ rises sharply and reaches its maximum around this temperature, accompanied by a displacement of the CIE coordinates from the green/yellow-green region toward red (Figure 3h). At higher temperatures, the Eu^{3+} emission also undergoes substantial thermal quenching, causing $I_{612\,nm}/I_{530\,nm}$ to decrease and the chromaticity trajectory to partially reverse. The separate evolution of the Mn^{2+} and Eu^{3+} emission intensities over 300–500 K further captures this differential quenching behavior (Figure S22). The temperature-dependent color variation therefore originates primarily from redistribution of the Mn^{2+} and Eu^{3+} emission contributions rather than from appreciable displacement of the Eu^{3+} peaks themselves. To rule out structural transformation as the origin of the luminescence variation, we further examined the thermal response at different heating rates. Continuous PL decay without abrupt spectral discontinuities is observed in BTP_2MnCl_4:Eu glasses at 10, 30, 60, and 100°C min^{-1} (Figure 3i and Figure S23). Together with the absence of detectable crystalline phases in the temperature-dependent PXRD measurements (Figure S4), these results indicate that the observed luminescence evolution primarily occurs within the amorphous glass matrix rather than being driven by a thermally induced glass-to-crystal transition [15, 33, 34].

To evaluate the energy conversion capability of BTP_2MnCl_4:Eu glasses under x-ray excitation, we systematically investigated their radioluminescence properties. X-ray absorption coefficient calculations based on the National Institute of Standards and Technology XCOM database reveal that both BTP_2MnCl_4 and its Eu-doped counterpart exhibit substantially higher x-ray absorption than the organic tetraphenylethylene (TPE)-based scintillator over a broad photon-energy range, with the attenuation efficiency increasing rapidly with thickness (Figure S24). Compared to the BTPCl host, which consists solely of low-Z elements, the incorporation of the $MnCl_2$ inorganic component significantly enhances x-ray stopping power, providing a solid foundation for efficient radiation energy deposition and luminescence conversion. Under x-ray excitation, BTP_2MnCl_4:Eu glasses retain the dual-emission characteristics of broadband Mn^{2+} green and sharp Eu^{3+} red (Figure 4a). As the Eu^{3+} doping content increases, the relative contribution of Eu^{3+} 4f–4f transitions progressively increases, accompanied by a displacement of the CIE coordinates from the green toward the orange-red region (Figure 4c). Meanwhile, Figure S25 further demonstrates that Eu^{3+} doping not only tailors the radioluminescence color but also modulates the overall emission intensity. Notably, the emission spectra of both Mn^{2+} and Eu^{3+} exhibit identical spectral profiles and peak positions under UV and x-ray excitation. This observation indicates that the radiative recombination pathways are essentially indistinguishable under the two excitation modalities.

Using LuAG:Ce (25 000 photons MeV^{-1}) as a reference [5, 35], the measured light yields of BTP_2MnCl_4:Eu glasses with nominal $EuCl_3{\cdot}6H_2O$ additions of 0, 0.1, 0.3, 0.5, and 1.0 mmol reach 18 843, 13 828, 8226, 8347, and 6586 photons MeV^{-1}, respectively (Figure 4b and Figure S26). Although this value is lower than the previously reported 26 000 photons MeV^{-1} for $(BnO\text{-}MTP)_2MnCl_4$ glass [18], the BTP_2MnCl_4 system was selected to balance glass-forming characteristics and scintillation performance, while providing a suitable host for incorporating additional lanthanide emissive centers. This material design strategy enables the development of multifunctional hybrid glass scintillators rather than solely optimizing scintillation light yield. The overall decrease in light yield with increasing Eu^{3+} content can be primarily attributed to enhanced nonradiative quenching and the competition between $Mn^{2+}\rightarrow Eu^{3+}$ energy transfer and radiative relaxation [17, 27, 29, 36]. As the Eu^{3+} concentration increases, the reduced separation between Eu^{3+} centers can facilitate energy migration and nonradiative relaxation, consistent with the observed Eu^{3+} concentration quenching and the decrease in thermal-quenching activation energy. Moreover, the high-frequency O–H vibrations identified by ATR-FTIR may provide an additional multi-phonon relaxation pathway. Consequently, the enhanced energy transfer from Mn^{2+} to Eu^{3+} cannot fully compensate for the increasing nonradiative losses, resulting in a reduction in overall scintillation efficiency. Notably, the light yield of BTP_2MnCl_4 surpasses the reported values for commercial scintillators such as $Y_3Al_5O_{12}$:Ce (16 400 photons MeV^{-1}) and $CdWO_4$ (13 000 photons MeV^{-1}) [37]. Although Eu^{3+} incorporation lowers the radioluminescence output, the Eu-doped glass still shows a light yield higher than that of the previously reported Eu-based hybrid glass (1419 photons MeV^{-1}) [27]. To assess the responsiveness of the glasses to varying radioluminescence, we further examined the integrated x-ray-excited luminescence (XEL) intensities as a function of x-ray dose rate. Both BTP_2MnCl_4 and BTP_2MnCl_4:Eu glasses exhibit good linear responses over the dose-rate range of 2.04–24.98 $mGy_{air}\ s^{-1}$, with their spectral profiles essentially unchanged (Figure 4d and Figure S26). The corresponding x-ray detection limits are as low as 26.7 and 92.6 $nGy_{air}\ s^{-1}$ (Figure S27), both far below the 5.5 $\mu Gy_{air}\ s^{-1}$ threshold required for medical diagnostic imaging [38]. Irradiation stability represents another critical parameter for the practical deployment of scintillating materials. The BTP_2MnCl_4:Eu glass maintains stable XEL responses over 60 consecutive x-ray on/off switching cycles and exhibits no discernible intensity degradation during prolonged irradiation at 30 kV and 26.6 mGy $_{air}\ s^{-1}$ (Figure 4e), indicating satisfactory radiation hardness.

Given the distinct thermal response characteristics observed for Mn^{2+} and Eu^{3+} emissions in the PL measurements, we further investigated the temperature-dependent XEL behavior. The radioluminescence of BTP_2MnCl_4:Eu evolves continuously with increasing temperature from 30°C to 150°C (Figure 4f and Figure S28), with the CIE coordinates shifting from the green/yellow-green toward the orange-red region. This evolution parallels the differential thermal quenching of the Mn and Eu channels discussed in Figure 3, indicating that temperature can also regulate their relative XEL contributions. Therefore, Eu^{3+}-doping introduces not only composition-dependent color tuning but also a temperature-responsive degree of freedom under x-ray excitation. To further verify the compositional versatility of this material design strategy, we conducted systematic investigations from two perspectives: dopant engineering and host-component expansion. Dy^{3+}-, Sm^{3+}-, and Eu^{3+}/Tb^{3+}-doped BTP_2MnCl_4 glasses exhibit characteristic lanthanide emissions

16163028, 0, Downloaded from https://advanced.onlinelibrary.wiley.com/doi/10.1002/adfm.79493 by Daqin Chen - Zhongshan University , Wiley Online Library on [05/11/2026]. See the Terms and Conditions (https://onlinelibrary.wiley.com/terms-and-conditions) on Wiley Online Library for rules of use; OA articles are governed by the applicable Creative Commons License

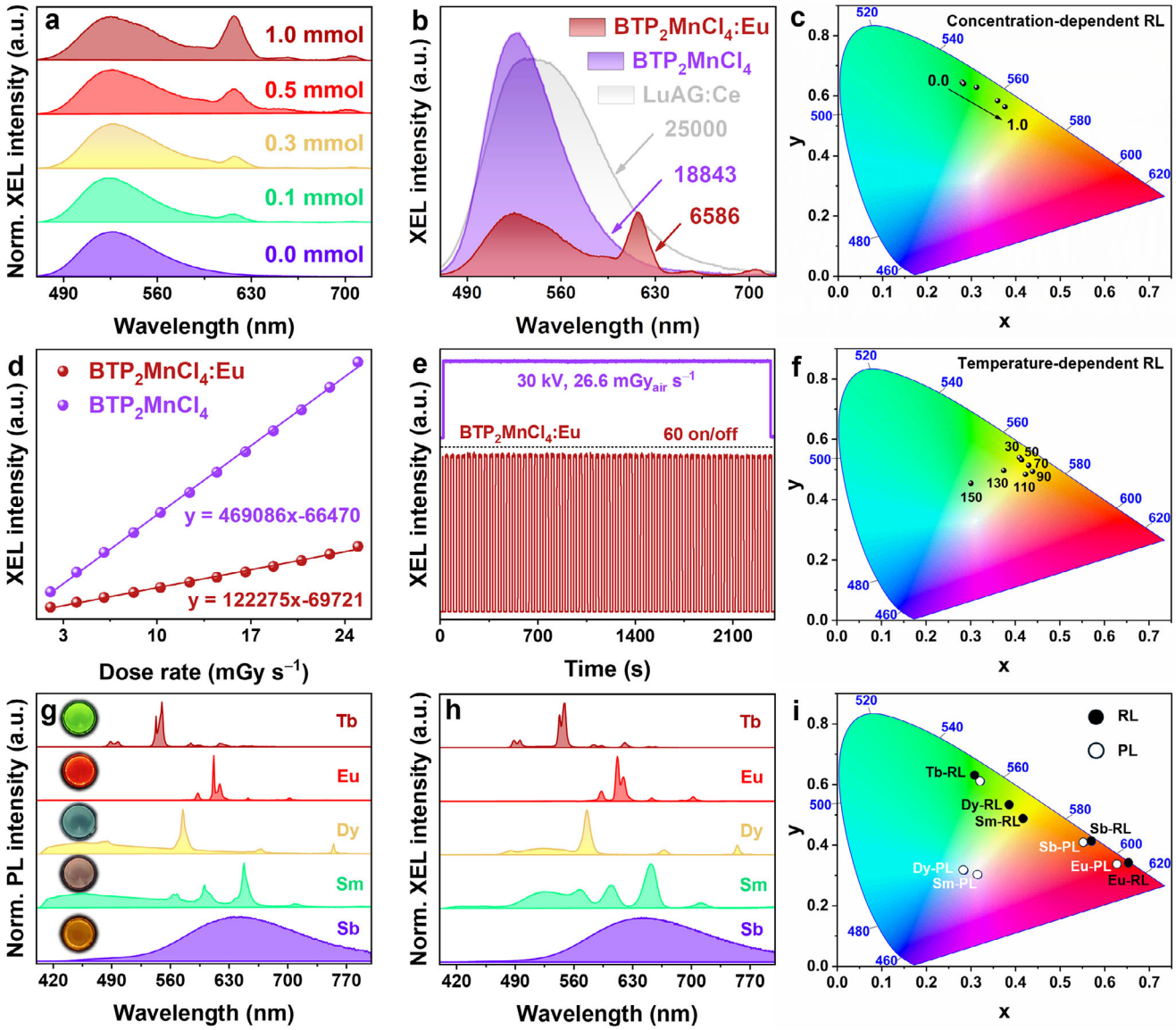


FIGURE 4 | X-ray scintillation properties and compositional versatility of hybrid metal-halide glasses. (a) Radioluminescence spectra of BTP_2MnCl_4:Eu glasses with nominal $EuCl_3{\cdot}6H_2O$ additions of 0–1.0 mmol under x-ray excitation. (b) Radioluminescence spectra of LuAG:Ce, BTP_2MnCl_4, and BTP_2MnCl_4:Eu with nominal 1.0 mmol $EuCl_3{\cdot}6H_2O$ addition at 30 kV and 19.9 mGy_{air} s^{-1}. (c) CIE chromaticity coordinates of BTP_2MnCl_4:Eu glasses with different Eu^{3+} contents under x-ray excitation. (d) Integrated x-ray-excited luminescence intensities of BTP_2MnCl_4 and BTP_2MnCl_4:Eu glasses as a function of x-ray dose rate. (e) Radioluminescence stability of BTP_2MnCl_4:Eu glass under 60 repeated x-ray on/off cycles and prolonged x-ray irradiation at 30 kV and 26.6 mGy_{air} s^{-1}. (f) Temperature-dependent CIE chromaticity coordinates of BTP_2MnCl_4:Eu glass from 30°C to 150°C under x-ray excitation at 30 kV and 26.6 mGy_{air} s^{-1}. (g) PL and (h) radioluminescence spectra for the directly synthesized Tb^{3+}-, Eu^{3+}-, Dy^{3+}-, Sm^{3+}-, and Sb^{3+}-based hybrid glasses. Insets in (g): photographs of the corresponding glasses under 365 nm excitation. (i) CIE chromaticity coordinates derived from the PL and radioluminescence spectra in (g) and (h).

across different regions of the CIE diagram (Figure S29). More broadly, directly synthesized Tb^{3+}-, Eu^{3+}-, Dy^{3+}-, Sm^{3+}-, and Sb^{3+}-based hybrid glasses exhibit characteristic PL and XEL spectra (Figure 4g,h) and cover a wide chromaticity range under x-ray excitation (Figure 4i). The PXRD patterns of all these glasses are dominated by broad diffuse features without observable crystalline diffraction peaks (Figure S30), confirming that the amorphous state is retained across these different emissive compositions. Furthermore, DSC measurements of representative Tb^{3+}- and Sb^{3+}-based glasses yield T_g/T_m ratios of 0.709 and 0.798, respectively (Figure S31), both exceeding the empirical threshold of 2/3 and indicating favorable glass-forming ability. These results show that the present glass-forming strategy is not confined to the Mn^{2+}/Eu^{3+} dual-emission system but is substantially compositionally extensible. This enables the incorporation of a broader spectrum of metal luminescent centers, thereby offering an expanded material palette for constructing tunable multicolor hybrid halide scintillators.

Optical transparency is a critical factor governing the spatial resolution of scintillation screens because internal scattering directly affects the lateral spreading of scintillation photons.

16163028, 0, Downloaded from https://advanced.onlinelibrary.wiley.com/doi/10.1002/adfm.79493 by Daqin Chen - Zhongshan University , Wiley Online Library on [05/11/2026]. See the Terms and Conditions (https://onlinelibrary.wiley.com/terms-and-conditions) on Wiley Online Library for rules of use; OA articles are governed by the applicable Creative Commons License

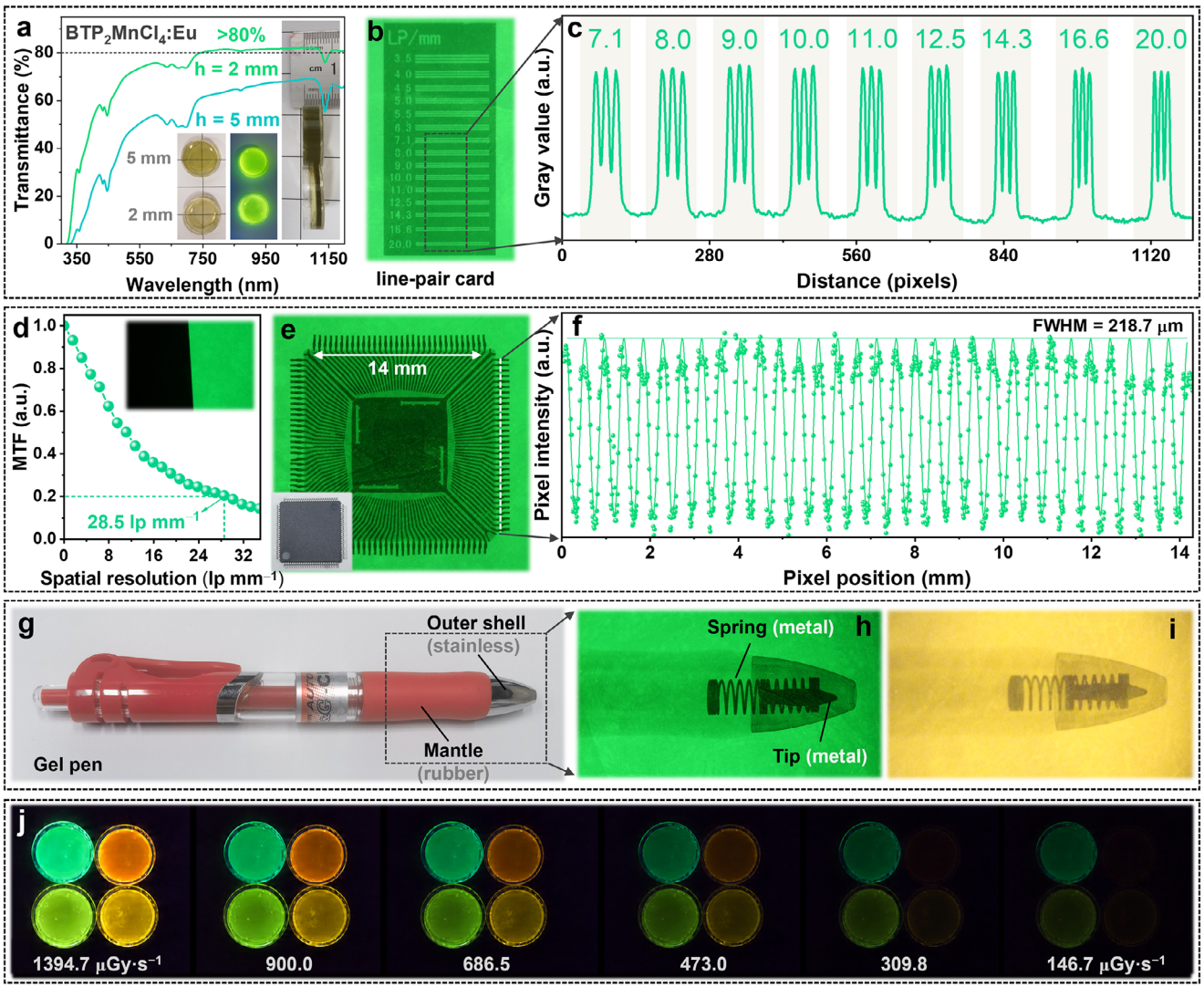


FIGURE 5 | Optical transparency and high-resolution x-ray imaging of BTP_2MnCl_4:Eu glass scintillators. (a) Optical transmittance spectra of BTP_2MnCl_4:Eu glasses containing 7.37 mol% Eu with different thicknesses. Insets: photographs of the glasses under daylight and 365 nm irradiation. (b) x-ray image of a standard line-pair test pattern acquired using a BTP_2MnCl_4 glass as a scintillation screen. (c) Grayscale intensity profiles extracted from the marked region in (b). (d) MTF obtained using the slanted-edge method for the BTP_2MnCl_4 glass. Inset: x-ray image of a lead plate with a sharp edge. (e) Optical and x-ray images of a microchip acquired using the BTP_2MnCl_4 scintillation screen. (f) Intensity profile extracted along the dashed line in (e) and corresponding Gaussian fit, giving an FWHM of 218.7 μm. (g) Photograph of the rubber mantle, metallic tip and spring, and stainless-steel outer shell of a gel pen. (h,i) X-ray images of the gel pen acquired using BTP_2MnCl_4 (h) and BTP_2MnCl_4:Eu containing 7.37 mol% (i) scintillation screens. (j) Radioluminescence photographs of compositionally distinct glass scintillators recorded at different x-ray dose rates.

The BTP_2MnCl_4:Eu glass maintains high transmittance even at millimeter-scale thicknesses. A 2 mm-thick sample exhibits a transmittance above 80% over 650–1200 nm, and the value remains above 60% when the thickness is increased to 5 mm (Figure 5a). This optical merit helps suppress scattering losses and mitigate optical crosstalk within the scintillation screen. We first evaluated the x-ray imaging resolution using a standard line-pair card. The BTP_2MnCl_4 glass clearly resolves line pairs up to 20 lp mm^{-1}, for which three well-separated response maxima remain distinguishable in the corresponding grayscale intensity profile (Figure 5b,c). Further analysis of the modulation transfer function (MTF) using the slanted-edge method gives a spatial resolution of 28.5 lp mm^{-1} at MTF = 0.2 (Figure 5d). Notably, this high spatial resolution is achieved with a 2 mm-thick glass screen, highlighting the advantage of the optically homogeneous amorphous matrix in suppressing particle-interface-induced scattering and maintaining imaging sharpness at millimeter-scale thicknesses.

To further validate the imaging capability of this scintillating screen for real-world complex objects, we selected a microchip and a gel pen containing components of different compositions. The imaging measurements were performed at an x-ray tube voltage of 50 kV and a dose rate of 24.98 mGy_{air} s^{-1}. As shown in Figure 5e, the x-ray image of the microchip clearly reveals its internal circuitry and periodic fine structures. Gaussian fitting of the intensity profile extracted along the white dashed line in the image yields an FWHM of 218.7 μm (Figure 5f), further illustrating the capability of the glass screen to resolve microscale structural features. For the gel pen, the rubber mantle, metallic

16163028, 0, Downloaded from https://advanced.onlinelibrary.wiley.com/doi/10.1002/adfm.79493 by Daqin Chen - Zhongshan University , Wiley Online Library on [05/11/2026]. See the Terms and Conditions (https://onlinelibrary.wiley.com/terms-and-conditions) on Wiley Online Library for rules of use; OA articles are governed by the applicable Creative Commons License

spring and tip, and stainless-steel outer shell produce distinct grayscale contrasts because of their different x-ray attenuation characteristics (Figure 5g). Both BTP_2MnCl_4 and BTP_2MnCl_4:Eu screens resolve the internal metallic parts (Figure 5h,i), indicating that the color modulation introduced by Eu^{3+} incorporation does not compromise the basic structural imaging performance. Beyond conventional grayscale imaging, the Mn^{2+}/Eu^{3+} dual-emission system also enables color-encoded visualization of radiation signals. As shown in Figure 5j, assembling glass units with different radioluminescence colors produces a spatially resolved multicolor radiation-response interface. As the x-ray dose rate decreases, the luminescence brightness in each region diminishes, while the color contrast remains discernible. The combination of composition-dependent color encoding and dose-dependent radioluminescence intensity therefore allows radiation information to be represented simultaneously through chromatic and brightness variations, providing a visual readout modality distinct from conventional monochromatic scintillators. Importantly, these composition-dependent radioluminescence characteristics arise from the same Mn^{2+}/Eu^{3+} emissive centers used for subsequent photonic authentication, establishing a direct material-level link between x-ray imaging and optical information encoding.

The preceding results show that Eu^{3+} content, excitation wavelength, and temperature can modulate both the emission color and spectral composition of BTP_2MnCl_4:Eu glasses, providing multiple dimensions for optical information encoding [4]. The moldability of the glasses further enables their processing into patterned and three-dimensional objects (Figure 6a,b). Notably, the bear-shaped glass exhibits a relatively uniform color distribution under daylight and 254 or 365 nm irradiation, whereas excitation at 300 and 310 nm produces a distinct local color contrast between the marked shoulder region and the surrounding area (Figure 6b), revealing wavelength-dependent spatial optical responses. On this basis, four glasses containing 0, 1.50, 3.97, and 7.37 mol% Eu^{3+} were selected as composition-encoded units, denoted X1–X4 (Figure 6c). By combining two excitation wavelengths (360 and 393 nm) with two temperatures (30°C and 80°C), a 4 × 2 × 2 composition-excitation-temperature optical response matrix was constructed. The four readout conditions are defined as state A (360 nm/30°C), state B (393 nm/30°C), state C (360 nm/80°C), and state D (393 nm/80°C) (Figure 6d). The corresponding CIE chromaticity coordinates further capture the evolution of the relative Mn^{2+} and Eu^{3+} emission contributions under these conditions (Figure S32 and Table S7).

Beyond simple color-based readout, the complementary broadband Mn^{2+} emission and multiple sharp Eu^{3+} characteristic lines provide distinct spectral channels within a single glass matrix. Their composition-, excitation-, and temperature-dependent intensity redistribution can be further translated into five-channel photonic barcodes for multilevel optical information authentication (Figure 6e). Specifically, S1 corresponds to the Mn^{2+} emission in the 470–580 nm region, while S2–S5 cover the Eu^{3+}-related spectral regions of 580–605, 605–630, 630–675, and 675–730 nm, respectively. The positions of the barcode elements are fixed by the predefined spectral channels, whereas their widths are determined by the corresponding normalized channel intensities. Accordingly, the four compositions under states A–D generate the composition-specific sub-barcodes A_1–A_4, B_1–B_4, C_1–C_4, and D_1–D_4, respectively (Figure 6f). Under 360 nm excitation, the Mn^{2+} channel retains a relatively large contribution, whereas switching to 393 nm markedly increases the weights of the Eu^{3+}-related channels. When heated to 80°C, the distinct thermal responses of the two emission centers further redistribute the spectral contributions across the channels. For each readout state, the four sub-barcodes derived from X_1–X_4 are sequentially integrated in equal spatial proportions (25% each) to yield barcode-A, barcode-B, barcode-C, and barcode-D (Figure S33). Details of the spectral processing and normalization procedure are provided in the Supporting Information, with the corresponding encoding parameters summarized in Table S8. These state-dependent photonic barcodes were further used to construct a sequential multilevel authentication scheme (Figure 6g). Barcode-A is initially scanned under state A and compared to its predefined reference fingerprint. Successful matching then validates barcodes B–D under states B, C, and D, in sequence. A mismatch at any stage terminates the authentication process, whereas successful matching across all four levels completes the verification. In this framework, Eu^{3+} composition defines the intrinsic material-encoding dimension, while excitation wavelength and temperature serve as external readout conditions that generate condition-dependent spectral fingerprints from the same composition array. To further evaluate the reversibility and reproducibility of the temperature-responsive optical encoding, we performed consecutive heating-cooling cycles between 30°C and 80°C on the same BTP_2MnCl_4:Eu glass. The PL spectra recorded under 360 and 393 nm excitation exhibit reproducible Mn^{2+} and Eu^{3+} emission profiles, with no obvious changes in their relative intensities or characteristic peak positions after repeated thermal cycling (Figures S34 and S35). These results demonstrate the reversible thermal modulation of the dual-emission response, supporting the reliability of the temperature-dependent photonic encoding strategy. Beyond conventional optical anti-counterfeiting, this strategy offers a potential route for built-in authentication of x-ray scintillation screens. Because the composition-dependent spectral fingerprints originate from the same Mn^{2+}/Eu^{3+} centers responsible for scintillation, the glass can simultaneously convert radiation into light and carry intrinsic optical identity information without additional labeling layers. Such spectral fingerprints could enable material identification and traceability through controlled UV excitation and temperature modulation, establishing a practical connection between x-ray imaging and photonic authentication.

3 | Conclusions

In summary, Ln^{3+}-doped BTP_2MnCl_4 transparent hybrid glass scintillators were fabricated by a one-step melt-quenching process, allowing direct shaping into diverse macroscopic forms. The BTP_2MnCl_4:Eu glasses exhibit dual emission from green Mn^{2+} and red Eu^{3+} centers, whose relative contributions can be tuned by Eu^{3+} content and excitation wavelength. PLE spectra and time-resolved PL decay measurements support $Mn^{2+}\rightarrow Eu^{3+}$ energy transfer and the involvement of Mn^{2+}-related excitation channels in Eu^{3+} emissions. Their distinct thermal responses further alter the Mn^{2+}/ Eu^{3+} emission balance, enabling multidimensional modulation of emission color and spectral output through composition, excitation wavelength, and temperature. Under x-ray excitation, the glasses retain their dual-emission characteristics,

16163028, 0, Downloaded from https://advanced.onlinelibrary.wiley.com/doi/10.1002/adfm.79493 by Daqin Chen - Zhongshan University , Wiley Online Library on [05/11/2026]. See the Terms and Conditions (https://onlinelibrary.wiley.com/terms-and-conditions) on Wiley Online Library for rules of use; OA articles are governed by the applicable Creative Commons License

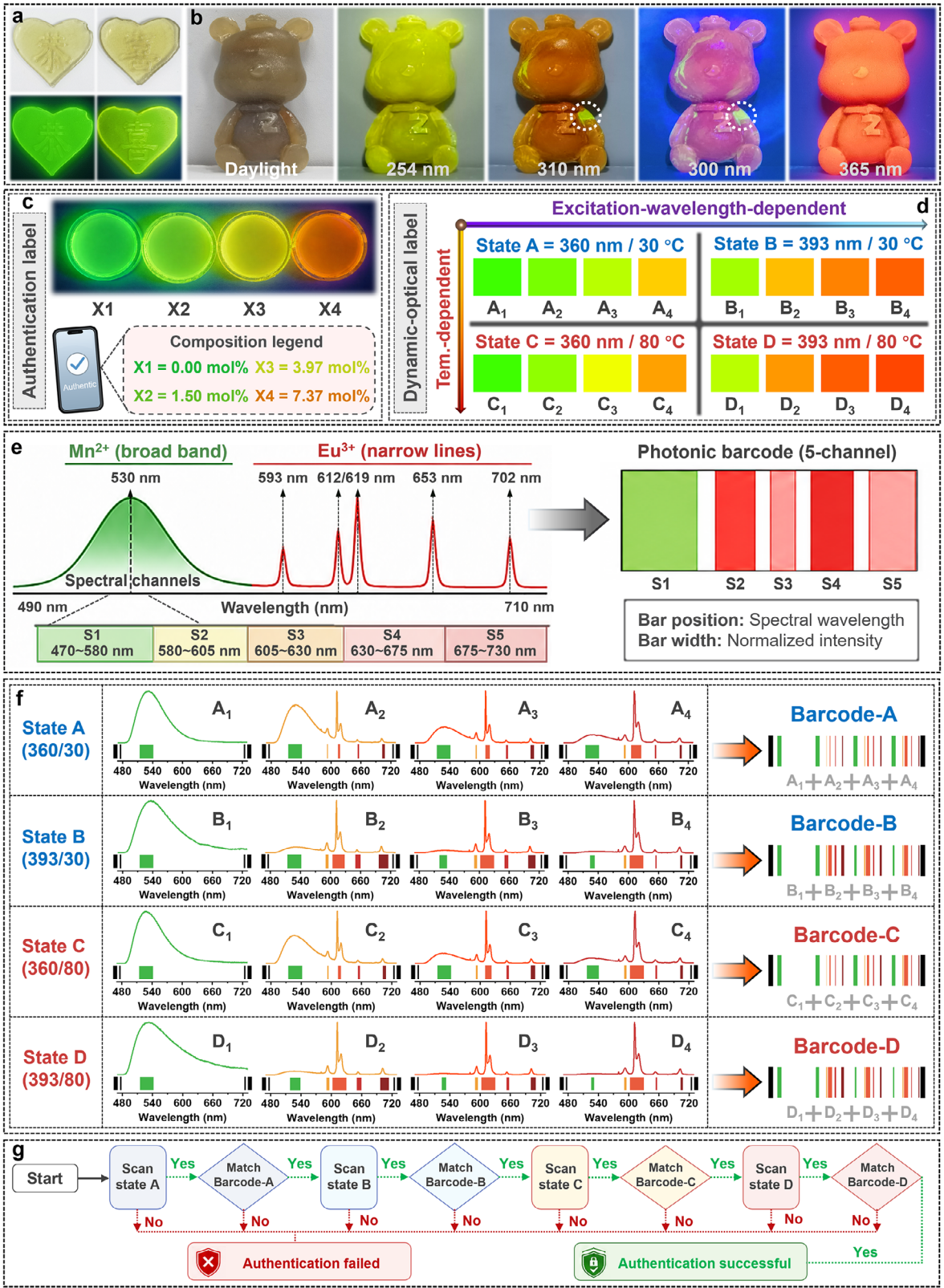


FIGURE 6 | Multilevel optical information encoding and photonic-barcode authentication of BTP_2MnCl_4:Eu glasses. (a) Photographs of BTP_2MnCl_4:Eu glasses under daylight and UV irradiation. (b) Photographs of a molded glass object under daylight and excitation at 254, 300, 310, and 365 nm. (c) Composition-coded optical units X1–X4 based on Eu^{3+} contents of 0, 1.50, 3.97, and 7.37 mol%, respectively. (d) Optical response states defined by four compositions, two excitation wavelengths (360 and 393 nm), and two temperatures (30°C and 80°C). (e) Conversion of the Mn^{2+}/Eu^{3+} emission spectrum into a five-channel photonic barcode. S1–S5 correspond to 470–580, 580–605, 605–630, 630–675, and 675–730 nm, respectively. (f) Emission spectra, corresponding composition-specific sub-barcodes, and integrated barcodes A–D under the four readout states. (g) Schematic workflow for sequential multilevel authentication based on matching of barcodes A–D.

16163028, 0, Downloaded from https://advanced.onlinelibrary.wiley.com/doi/10.1002/adfm.70493 by Daqin Chen - Zhongshan University , Wiley Online Library on [05/11/2026]. See the Terms and Conditions (https://onlinelibrary.wiley.com/terms-and-conditions) on Wiley Online Library for rules of use; OA articles are governed by the applicable Creative Commons License

together with effective radiation-energy conversion and stable dose-dependent responses. The fabricated glasses achieve a light yield of 18 843 photons MeV^{-1} and an x-ray detection limit of 26.7 nGy_{air} s^{-1}, while maintaining stable radioluminescence under repeated and prolonged irradiation. The BTP_2MnCl_4 scintillation screen achieves an imaging resolution of 28.5 lp mm^{-1} at MTF = 0.2 and resolves internal features of representative objects. In addition, composition-dependent radioluminescence colors combined with dose-dependent brightness provide a multicolor visual readout of radiation-response information. The extension to additional emissive metal centers further demonstrates the compositional adaptability of this glass-forming strategy. Finally, the composition-, excitation-, and temperature-dependent spectral responses were converted into state-specific photonic barcodes for sequential multilevel authentication. Overall, these results establish hybrid metal-halide glasses as a versatile platform that integrates x-ray scintillation and imaging with multidimensional spectral information encoding, offering a potential route to scintillation screens with intrinsic optical authentication capabilities. This multifunctional design further expands the application scope of hybrid glass scintillators and offers new opportunities for next-generation intelligent scintillation materials, including environment-responsive adaptive scintillators and information-integrated radiation detection components.

Author Contributions

Shilin Jin: conceptualization, writing – original draft, investigation, formal analysis, visualization. **Xiaoai Cao**: data curation, validation. **Luyao Wei**: validation, methodology. **Zhiqiong Wu**: validation, data curation. **Daqin Chen**: writing – review and editing, resources, supervision, funding acquisition, visualization.

Acknowledgements

This research was supported by the National Natural Science Foundation of China (Nos. 52572155 and 52272141) and Natural Science Foundation of Fujian Province (No. 2024J02014).

Conflicts of Interest

The authors declare no conflicts of interest.

Data Availability Statement

The data that support the findings of this study are available from the corresponding author upon reasonable request.

References

1. X. Ou, X. Qin, B. Huang, et al., "High-Resolution X-ray Luminescence Extension Imaging," *Nature* 590 (2021): 410–415, https://doi.org/10.1038/s41586-021-03251-6.

2. C. Roques-Carmes, N. Rivera, A. Ghorashi, et al., "A Framework for Scintillation in Nanophotonics," *Science* 375 (2022): abm9293, https://doi.org/10.1126/science.abm9293.

3. J. Qiu, C. Gu, M. Chen, et al., "Scattering-Free Lanthanide-Ionic Liquid Scintillators for High-Resolution and Adaptive X-ray Imaging," *Nature Communications* 16 (2025): 11609, https://doi.org/10.1038/s41467-025-66754-0.

4. H. Li, Q. Dong, J. Guo, et al., "A Smart-Perception Rare Earth MOF," *Advanced Materials* 38 (2026): 21289, https://doi.org/10.1002/adma.202521289.

5. L. Xu, P. Ran, W. Zhou, et al., "All-Inorganic Metafabric Scintillators for Conformally Flexible and Wearable X-ray Detection and Imaging," *Science Advances* 11 (2025): adv5537, https://doi.org/10.1126/sciadv.adv5537.

6. Y. C. Kim, K. H. Kim, D.-Y. Son, et al., "Printable Organometallic Perovskite Enables Large-Area, Low-Dose X-ray Imaging," *Nature* 550 (2017): 87–91, https://doi.org/10.1038/nature24032.

7. X. Li, X. Luo, C. Li, et al., "Organic Scintillators for Next-Generation Radiation Detection: Principles of Molecular Design, Mechanisms, and Emerging Applications," *Matter* 9 (2026): 102715, https://doi.org/10.1016/j.matt.2026.102715.

8. M. L. Zaffalon, L. Gironi, M. Nikl, and S. Brovelli, "From Optoelectronics to Radiation Detection: Light Yield Challenges in Perovskite Scintillators," *ACS Energy Letters* 11 (2026): 31–42, https://doi.org/10.1021/acsenergylett.5c03188.

9. D. H. Kong, Y. Zhou, Z. N. Chen, and L. J. Xu, "Manganese(II)-Based Luminescent Materials for Advanced Scintillation," *Advanced Functional Materials* 36 (2026): 75222, https://doi.org/10.1002/adfm.75222.

10. L. Xu, Y. Li, Q. Guan, et al., "Molecular-Driven Lead-Free Halide Photoferroelectric Solid Solution for High-Temperature Sensitive Self-Powered X-ray Detection," *Science Advances* 12 (2026): aef7693, https://doi.org/10.1126/sciadv.aef7693.

11. H. Cui, W. Li, Q. Li, et al., "Highly Luminescent Organic-Inorganic Hybrid Antimony Halide Scintillators for Real-Time Dynamic and 3D X-ray Imaging," *Light: Science & Applications* 15 (2026): 88, https://doi.org/10.1038/s41377-025-02152-x.

12. W. Tian, H. Zhang, X. Qian, et al., "Pixel-Level X-Ray to NIR Image Fusion Based on Lead-Free Halide Perovskite for Biological Imaging," *Advanced Functional Materials* 36 (2026): 75002, https://doi.org/10.1002/adfm.75002.

13. H. Lian, R. Kuang, M. Gao, S. Tao, J. Nie, and J. Wang, "Efficient Rare-Earth-Based Hybrid Metal Halide Single-Crystal Scintillators Enabled by Antimony-Assisted Triplet Exciton-Harvesting," *Angewandte Chemie International Edition* 65 (2026): 2103432, https://doi.org/10.1002/anie.2103432.

14. T. Feng, Z. Zhou, Y. An, et al., "Large-Area Transparent Antimony-Based Perovskite Glass for High-Resolution X-ray Imaging," *ACS Nano* 18 (2024): 16715–16725, https://doi.org/10.1021/acsnano.4c01761.

15. Z. Zhou, J. Zheng, S. Ruan, et al., "A Transparent Hybrid Metal Halide Glassy Scintillation Screen for High-Resolution Fast Neutron Radiography," *Nature Communications* 16 (2025): 6215, https://doi.org/10.1038/s41467-025-61503-9.

16. Z.-Y. Li, R. Feng, Z.-G. Li, et al., "Glass Formation in Hybrid Metal Halides via Breaking Molecular Rotational Order," *Nature Communications* 17 (2026): 1850, https://doi.org/10.1038/s41467-026-68563-5.

17. Z.-L. He, J.-B. Luo, J.-H. Chen, et al., "A Universal Strategy toward Two-Component Organic-Inorganic Metal Halide Luminescent Glasses and Glass-Crystal Composites," *Science Advances* 11 (2025): adu1982, https://doi.org/10.1126/sciadv.adu1982.

18. Q. Qiu, G. Zhang, J. Chen, et al., "Organic Phosphonium Side-Chain Engineering in Metal Halide Glassy Scintillators for Enhanced X-Ray Dynamic Imaging," *Small* 21 (2025): 2407346, https://doi.org/10.1002/smll.202407346.

19. Q. P. Peng, Z. L. He, J. H. Chen, et al., "Organic-Inorganic Metal Halide Glass Optical Fibers for Ultralow-Loss and Bendable Photonic Applications," *Matter* 8 (2025): 102277, https://doi.org/10.1016/j.matt.2025.102277.

20. Z.-L. He, J.-H. Chen, T.-C. Wang, Q.-P. Peng, J.-H. Wei, and D.-B. Kuang, "Tailoring Hybrid Copper Iodide Cluster Glasses via Ligand Design for Stable Multifunctional X-Ray Imaging," *Angewandte Chemie International Edition* 65 (2026): 9659580, https://doi.org/10.1002/anie.9659580.

16163028, 0, Downloaded from https://advanced.onlinelibrary.wiley.com/doi/10.1002/adfm.79493 by Daqin Chen - Zhongshan University , Wiley Online Library on [05/11/2026]. See the Terms and Conditions (https://onlinelibrary.wiley.com/terms-and-conditions) on Wiley Online Library for rules of use; OA articles are governed by the applicable Creative Commons License

21. Y. Wang, P. Dang, Z. Zeng, et al., "Sensitizing effect of lanthanide luminescence by Mo^{4+}/Ag^{+} in double perovskites: Great enhancement of near-infrared emission via wide range of excitation (250–850 nm)," *Light: Science & Applications* 15 (2026): 87, https://doi.org/10.1038/s41377-025-02159-4.

22. S. Jin, M. Zhang, L. Zeng, and D. Chen, "Lanthanide-Doped Lead-Free Halide Double Perovskites: Optical Synergy, Performance Engineering, and Multifunctional Optoelectronics," *Advanced Functional Materials* 36 (2026): 32102, https://doi.org/10.1002/adfm.202532102.

23. B. Li, Y. Wang, Y. Xu, and Z. Xia, "Emerging 0D Hybrid Metal Halide Luminescent Glasses," *Advanced Materials* 37 (2025): 2415483, https://doi.org/10.1002/adma.202415483.

24. W. Cai, C. Li, Q. Guo, F. Ji, M. Zhang, and Y. Zhan, "Modulation of Trichromatic Emission Centers in Organic–Inorganic Hybrids for Optoelectronic Applications," *Nano-Micro Letters* 18 (2026): 140, https://doi.org/10.1007/s40820-025-01965-0.

25. J. Fan, H. Li, W. Liu, and G. Ouyang, "Fabrication Strategies of Mn^{2+}-Based Scintillation Screens for X-Ray Detection and Imaging," *Angewandte Chemie International Edition* 64 (2025): 202425661, https://doi.org/10.1002/anie.202425661.

26. J.-H. Chen, Z.-L. He, Q.-P. Peng, et al., "Thermal Property Engineering in Mn-Based Hybrid Halides via Structural Tailoring of Phosphonium Cations," *Angewandte Chemie International Edition* 65 (2026): 21897, https://doi.org/10.1002/anie.202521897.

27. T. C. Wang, Z. L. He, J. B. Luo, et al., "Organic-Inorganic Hybrid Rare Earth Halide Glasses for Tunable Multicolor X-ray Scintillation," *Angewandte Chemie International Edition* 64 (2025): 202504658, https://doi.org/10.1002/anie.202504658.

28. W. Li, H. Wu, Y. Huang, et al., "Ultra-Fast-Healing Glassy Hyperbranched Plastics Capable of Restoring 26.4 MPa Tensile Strength within One Minute at Room Temperature," *Angewandte Chemie International Edition* 63 (2024): 202408250, https://doi.org/10.1002/anie.202408250.

29. L. Lian, D. Xiong, Y. Fan, et al., "Water-Assisted Rapid Evaporation Synthesis of Transparent and Multicolor Luminescent Lanthanide-Based Metal Halide Glasses for High-Resolution X-Ray Imaging," *Advanced Functional Materials* 36 (2025): 23727, https://doi.org/10.1002/adfm.202523727.

30. X. Wei, J. Chen, Q. Xu, et al., "Chain-Mobility-Enabled 1D Lanthanide Coordination Polymer Glassy Scintillators for Underwater X-Ray Videography," *Advanced Materials* 38 (2026): 73911, https://doi.org/10.1002/adma.73911.

31. H. Yang, H. Lu, X. Wang, et al., "Recyclable Luminescent Solar Concentrator from Lead-Free Perovskite Derivative," *Light: Science & Applications* 14 (2025): 297, https://doi.org/10.1038/s41377-025-01973-0.

32. S. Jin, S. Zhu, L. Wei, et al., "Near-Infrared Emitting Lead-Free Perovskite Scintillators for X-Ray Imaging with Suppressed Optical Crosstalk," *Laser & Photonics Reviews* 20 (2025): 02436, https://doi.org/10.1002/lpor.202502436.

33. H. Zhang, X. Huang, T. Wan, et al., "Integrated Copper-Halide Activated Scintillator Fiber Array for Remote High-Resolution X-ray Imaging," *Nature Communications* 16 (2025): 5973, https://doi.org/10.1038/s41467-025-61416-7.

34. Z.-L. He, Y.-X. Luo, J.-H. Chen, et al., "Molecular Design-Enabled Pyridinium-Based Metal Halide Glass Scintillators with Robust Glass-Forming Ability and Tailorable Radioluminescence," *Angewandte Chemie International Edition* 64 (2025): 202518282, https://doi.org/10.1002/anie.202518282.

35. G. Xing, B. Chen, Y. Wang, et al., "Molecularly Engineered Spherical Hybrid Glass Scintillator Enables Portable Omnidirectional X-Ray Detection With High Sensitivity," *Advanced Materials* 38 (2026): 17821, https://doi.org/10.1002/adma.202517821.

36. Y. Wen, Y. Xu, X. Zhang, et al., "Phase Control via Composite Encapsulation for Ultra-Stable, High-Resolution Organic Manganese Halide Scintillator Array," *Advanced Materials* 37 (2025): 07021, https://doi.org/10.1002/adma.202507021.

37. Q. Huang, S. Jin, L. Wei, et al., "Transparent Hybrid Metal Halide Glassy Scintillators for Tunable Multicolor and High-Resolution X-ray Imaging," *Journal of Advanced Ceramics* 15 (2026): 9221317, https://doi.org/10.26599/jac.2026.9221317.

38. R. Li, Y. Jiao, W. Zhu, et al., "Ultrabright X-ray Scintillators Enabled by Strong Exciton Confinement and Hierarchical Energy Funneling," *Advanced Functional Materials* 36 (2026): 32084, https://doi.org/10.1002/adfm.202532084.

Supporting Information

Additional supporting information can be found online in the Supporting Information section.

Supporting File 1: adfm79493-sup-0001-SuppMat.docx.

Supporting File 2: adfm79493-sup-0002-SuppMat.docx.

16163028, 0, Downloaded from https://advanced.onlinelibrary.wiley.com/doi/10.1002/adfm.79493 by Daqin Chen - Zhongshan University , Wiley Online Library on [05/11/2026]. See the Terms and Conditions (https://onlinelibrary.wiley.com/terms-and-conditions) on Wiley Online Library for rules of use; OA articles are governed by the applicable Creative Commons License